OPEN

# A dye-sensitized visible light photocatalyst-Bi$_{24}$O$_{31}$Cl$_{10}$

Liang Wang[1]*, Jun Shang[1]*, Weichang Hao[1,2], Shiqi Jiang[1], Shiheng Huang[1], Tianmin Wang[1], Ziqi Sun[2], Yi Du[2], Shixue Dou[2], Tengfeng Xie[3], Dejun Wang[3] & Jiaou Wang[4]

[1]Center of Materials Physics and Chemistry and Department of Physics, Beihang University, Beijing 100191, P. R. China, [2]Institute for Superconducting and Electronic Materials, University of Wollongong, Wollongong NSW 2522, Australia, [3]College of Chemistry, Jilin University, Changchun 130012, P. R. China, [4]Beijing Synchrotron Radiation Facility, Institute of High Energy Physics, Chinese Academy of Sciences, Beijing 100049, P. R. China.

The *p*-block semiconductors are regarded as a new family of visible-light photocatalysts because of their dispersive and anisotropic band structures as well as high chemical stability. The bismuth oxide halides belong to this family and have band structures and dispersion relations that can be engineered by modulating the stoichiometry of the halogen elements. Herein, we have developed a new visible-light photocatalyst Bi$_{24}$O$_{31}$Cl$_{10}$ by band engineering, which shows high dye-sensitized photocatalytic activity. Density functional theory calculations reveal that the *p*-block elements determine the nature of the dispersive electronic structures and narrow band gap in Bi$_{24}$O$_{31}$Cl$_{10}$. Bi$_{24}$O$_{31}$Cl$_{10}$ exhibits excellent visible-light photocatalytic activity towards the degradation of Rhodamine B, which is promoted by dye sensitization due to compatible energy levels and high electronic mobility. In addition, Bi$_{24}$O$_{31}$Cl$_{10}$ is also a suitable photoanode material for dye-sensitized solar cells and shows power conversion efficiency of 1.5%.

The exploration of novel visible-light-driven photocatalysts is required to meet growing demands in environmental pollution purification[1–3] and energy conversion[4,5], which remains a most essential challenge. Considering the visible-light photocatalysis, the potential photocatalysts must satisfy several criteria with respect to electronic structure: (i) narrow band gap (<3.0 eV) for absorption of visible light, (ii) high quantum conversion efficiency, (iii) efficient separation of photoexcited electrons and holes, (iv) capability for photoexcited charge carrier transfer and (v) chemical stability against photocorrosion in photocatalysis[6]. Recently, *p*-block-element based materials (*p*-block compounds) have been found to be a new family of visible-light photocatalysts[7–9]. Some of them have demonstrated excellent photocatalytic properties towards degradation of organics and water splitting even better than the conventional wide-band-gap transition metal oxides (*d*-block compounds)[9,10]. The unexpected photocatalytic properties of these *p*-block compounds are attributed to their unique band structures that fulfil the electronic-structure prerequisites for visible-light photocatalysis. For example, it has been proven that the band gap can be narrowed if *p*-block elements participate in the formation of the top energy level of the valence band (VB) or the bottom energy level of the conduction band (CB)[11] (Supplementary Figure S1). In addition, the *d* orbital in *p*-block compounds do not participate in the band edge and only form deep energy levels, because the *d* orbital is either empty (d^0) or completely filled (d^{10}) in *p*-block compounds[12]. The VB and CB in *p*-block compounds are therefore only constructed from *p* states or *sp* states. The anisotropic properties of *p* and *sp* states lead to highly dispersive band structures[13]. As a result, the effective mass of charge carriers is much smaller, which facilitates photo-induced charge carrier transfer in photocatalysis[14–16]. Although *p*-block photocatalysts possess promising electronic characteristics[7,11], their limited absorption range of visible light and chemical instability in photocatalysis are obstructing their further photocatalytic applications.

Band engineering is an effective approach to improve the photocatalytic activity of semiconductors. The band gap and quantum conversion efficiency can be modulated by the particle size and dimensions of the photocatalyst. The separation and transfer of photoexcited charge carriers can be promoted by chemical modification of electronic structures. The light absorption range, on the other hand, can be extended by photosensitization[17,18]. It is widely accepted that dye molecules enhance the visible light absorption of sensitized photocatalysts by injecting electrons from the lowest unoccupied molecular orbital (LUMO) of excited dye into the CB of the photocatalyst[19]. Semiconductors which are able to satisfy the above band engineering criteria are desirable for the development of visible-light photocatalysts.
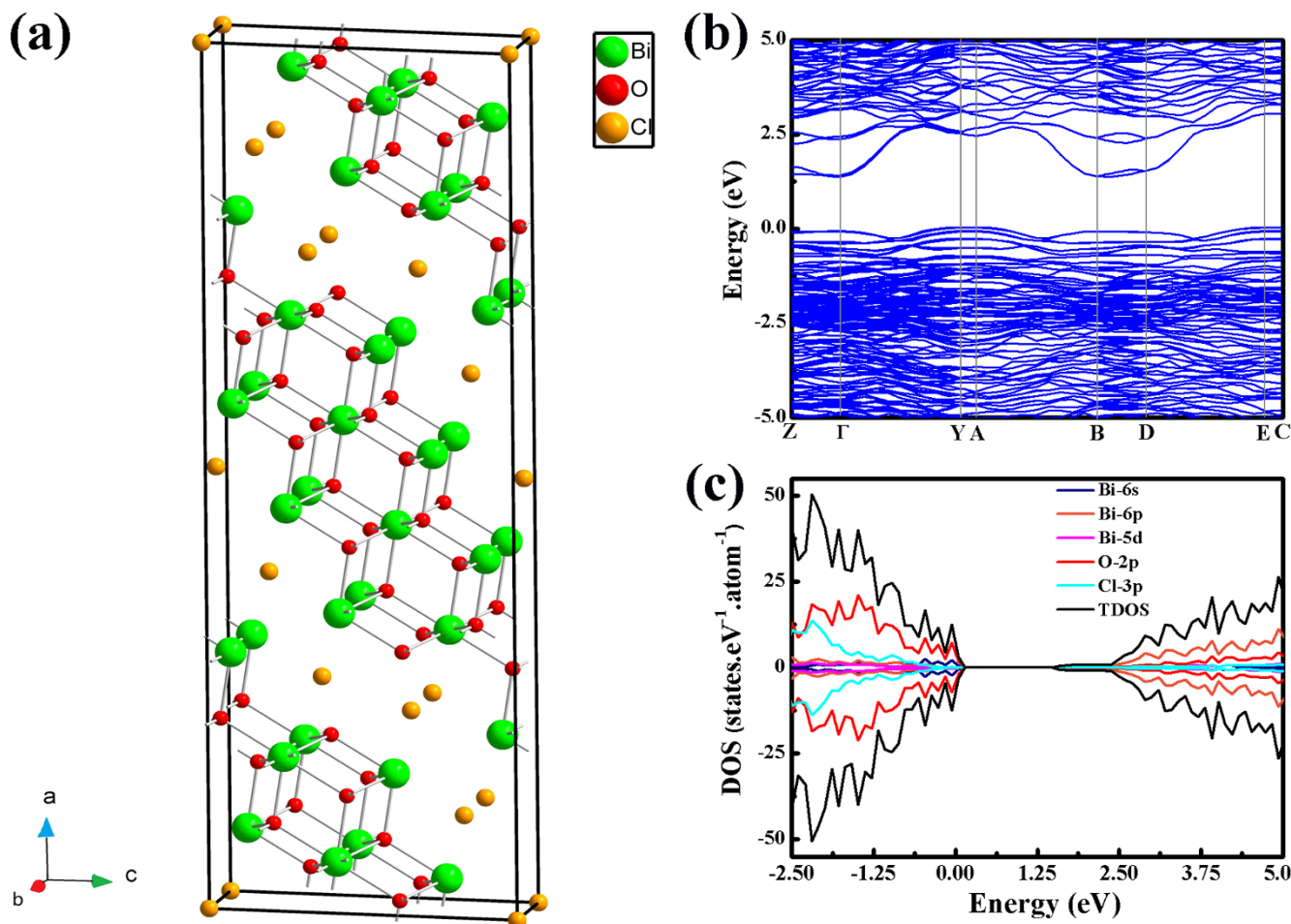
Figure 1 | DFT calculations of crystal and electronic structures for $Bi_{24}O_{31}Cl_{10}$. (a)Simulated crystal structure of $Bi_{24}O_{31}Cl_{10}$, in which Bi_2O_2 stacks are separated by Cl layers. Green, yellow, and red balls represent Bi, Cl, and O, respectively. (b) Calculated band structure of $Bi_{24}O_{31}Cl_{10}$ shows a very dispersive CB structure that consists of Bi 6p and O 2p orbitals. (c) Calculated density of states (DOS) of $Bi_{24}O_{31}Cl_{10}$ indicates a band gap of 2.20 eV.

Recently, considerable attention has been drawn to the bismuth-based semiconductors. It has been found that many Bi-based compounds possess a narrow band gap and exhibit high visible-light photocatalytic activity because of their hybridized O 2p and Bi $6s^2$ valence bands[20]. Therefore Bi-based compounds have attracted much research interest in terms of their synthesis, characterization and photocatalytic properties, and they have become an important family of visible light photocatalysts. The recently reported Bi-based compounds include Bi_xMO_y (Bi_2O_3, Bi_2S_3, Bi_2WO_6, $Bi_{12}GeO_{20}$, $Bi_4Ti_3O_{12}$, Bi_2MoO_6, $BiVO_4$, $Bi_2O_2CO_3$)[21–28], BiOX (BiOCl, BiOBr, BiOI)[29] and O-rich BiOX compounds ($Bi_{24}O_{31}Br_{10}$, Bi_3O_4Cl, $Bi_{12}O_{17}Cl_2$, Bi_3O_4Br, Bi_5O_7I)[9,30–32], and $MBiO_3$ ($NaBiO_3$, $KBiO_3$, $LiBiO_3$, $AgBiO_3$)[33–35] and they can generally be classified as binary oxides or sulfides, multi-component oxides or oxyhalides. Among them, the bismuth oxide halides ($Bi_xO_yX_z$, X is a halogen element) are such materials, and are regarded as the most promising family of visible-light p-block photocatalysts due to their readily tunable electronic structure as well as their high chemical stability. Their band structures and dispersion relations can be precisely engineered by modulating the stoichiometry of the halogen element[9,36]. Moreover, their two-dimensional (2D) layered structure enables $Bi_xO_yX_z$ to form thin nanosheets with a high surface area that further facilitates photocatalytic efficiency[37].

In this work, the p-block photocatalyst $Bi_{24}O_{31}Cl_{10}$ with high dye-sensitized visible-light photocatalytic activity was discovered by band design and engineering. It was found that the excellent photocatalytic properties of $Bi_{24}O_{31}Cl_{10}$ originated from its anisotropic and highly

dispersive electronic structure, and they can be further promoted by photosensitization. It is suggested that $Bi_{24}O_{31}Cl_{10}$ is also a candidate material as a photoanode in dye sensitized solar cells (DSSCs) which is attributed to its suitable energy levels and high electronic mobility.

Results and Discussion

Crystal and electronic structures of $Bi_{24}O_{31}Cl_{10}$. The crystal and electronic structures are of great importance for photocatalytic properties. We carried out density functional theory (DFT) calculations to reveal the detailed electronic structures of $Bi_xO_yCl_z$ compounds by tuning the stoichiometric ratio of chlorine, in order to explore potential candidate compounds for photocatalysts. $Bi_{24}O_{31}Cl_{10}$, a compound which has a monoclinic structure with space group A12/m1 (JCPDS 75-0887)[38], exhibits promising crystal and electronic structures for photocatalysis. Its crystal structure consists of stair-like [Bi,O] layers connected to the shared Cl^-, as shown in Figure 1(a). The Bi, Cl, and O atoms fit into a layered stacking model. The calculated band structure and density of states (DOS) indicate that the CB of $Bi_{24}O_{31}Cl_{10}$ mainly consists of hybridized Bi 6p and O 2p orbitals, whereas the VB is contributed by hybridized Bi 6s, Cl 3p, and O 2p orbitals, as shown in Figure 1(b) and (c). The calculations suggest that $Bi_{24}O_{31}Cl_{10}$ is a direct-band-gap semiconductor with a gap of 2.20 eV. It is worth noting that first-principles calculations generally underestimate the band-gap value. The gap of $Bi_{24}O_{31}Cl_{10}$ was determined to be 2.80 eV in our experiments, which confirms that this compound can absorb visible light (see the section on photocatalytic properties of $Bi_{24}O_{31}Cl_{10}$ below). Interestingly, the

bottom of the CB and the top of the VB in $Bi_{24}O_{31}Cl_{10}$ are only constructed from p and sp states, which exactly satisfy the band requirements of p-block photocatalysts. This is evidenced by the dispersive CB and VB in $Bi_{24}O_{31}Cl_{10}$, as shown in Figure 1(b). This gives photo-excited charge carriers small effective mass, which has benefits for charge transport under irradiation. In addition, separation of photo-induced electron-hole pairs is expected to be promoted by charge transfer from the sp-state VB and p-states CB in $Bi_{24}O_{31}Cl_{10}$ due to orbital asymmetry in real space[39]. The unique crystal and electronic structures of $Bi_{24}O_{31}Cl_{10}$ indeed lead to excellent photocatalytic performances, which have been demonstrated experimentally in this work.

Figure 2(a) and (b) shows typical X-ray diffraction (XRD) patterns and scanning electron microscope (SEM) images of as-prepared $Bi_{24}O_{31}Cl_{10}$ samples. It reveals plate-like particles in sizes of several hundred nanometers and thicknesses of 50–100 nm. The post-annealing process is found to be critical for the morphology and the size of $Bi_{24}O_{31}Cl_{10}$ particles. The particles become significantly larger and agglomerate as the annealing temperature is increased above 700°C, which potentially suppresses photocatalytic performance (See Supporting Information). In this work, all the results are obtained from the $Bi_{24}O_{31}Cl_{10}$ sample annealed at 600°C. X-ray photoelectron spectroscopy (XPS) results for $Bi_{24}O_{31}Cl_{10}$ are shown in Supplementary Figure S2(a), in which the peaks for Bi 4f, Bi 5d, O 1s, and Cl 3d orbitals are identified. The Bi peaks correspond to Bi $4f_{7/2}$ and Bi $4f_{5/2}$, which are located at 158.76 eV and 163.88 eV, respectively (with the splitting energy $\Delta = 5.12$ eV), as shown in Supplementary Figure S2(b), indicating that Bi only presents a valence of $+3$ in $Bi_{24}O_{31}Cl_{10}$[40].

Photocatalytic properties of $Bi_{24}O_{31}Cl_{10}$. The visible light photocatalytic activity of the $Bi_{24}O_{31}Cl_{10}$ was evaluated by a standard Rhodamine B (RhB) degradation measurement (Supplementary Figure S3(a) and (b)). In the photocatalytic degradation of RhB, the activities of $Bi_{24}O_{31}Cl_{10}$, BiOCl, Bi_2O_3 and N-doped TiO_2 are compared in Figure 3(a) and (b). $Bi_{24}O_{31}Cl_{10}$ catalyst shows higher photo-oxidation activity than BiOCl, Bi_2O_3, N-doped TiO_2. After irradiation for 60 min, the removal ratio on the $Bi_{24}O_{31}Cl_{10}$ sample reaches 95%, while only 15%, 88% and 70% RhB removal for Bi_2O_3, BiOCl and N-doped TiO_2, respectively. The removal of total organic carbon (TOC) was chosen as a mineralization index to characterize the RhB degradation. The time independence of the TOC data in the RhB solution in the presence of the $Bi_{24}O_{31}Cl_{10}$ catalyst under visible light irradiation is shown in Supplementary Figure S4. It is observed that 42% of the TOC was eliminated after

105 min of irradiation, indicating that RhB could be mineralized in this process. The durability and stability of the $Bi_{24}O_{31}Cl_{10}$ were characterized by a cycling test of photodegradation, in which $Bi_{24}O_{31}Cl_{10}$ demonstrates high photocatalytic activity in five runs (shown in Supplementary Figure S5). XRD patterns of $Bi_{24}O_{31}Cl_{10}$ collected before and after photodegradation indicate that this compound is very stable during the photocatalytic process (shown in Supplementary Figure S6).

Figure 3(c) shows the ultraviolet-visible (UV-Vis) diffuse reflectance spectrum of $Bi_{24}O_{31}Cl_{10}$ powder. It reveals an absorption edge of 445 nm with a tail extending to 480 nm. This is consistent with the yellow color of the powder (Figure 3(c) inset), which indicates that $Bi_{24}O_{31}Cl_{10}$ could efficiently absorb visible light. According to the Tauc formula[41], $Bi_{24}O_{31}Cl_{10}$ possesses a direct band gap of 2.80 eV (Figure 3(c) inset).

We carried out Mott-Schottky measurements on the $Bi_{24}O_{31}Cl_{10}$ sample in order to reveal the fine electronic structure, such as the positions of the energy levels. Typical Mott-Schottky plots collected in the dark for $Bi_{24}O_{31}Cl_{10}$ are presented in Figure 3(d). We found that the slope of the linear $1/C^2$ potential curve, where C is the capacitance, was positive, indicating that $Bi_{24}O_{31}Cl_{10}$ has a n-type semiconductor characteristic[42,43]. It is well known that the bottom of the CB of n-type semiconductors is more negative by about -0.1 V than the flat band potential (V_{fb})[43]. The V_{fb} value of $Bi_{24}O_{31}Cl_{10}$ was determined to be about -0.73 V versus $Hg/HgCl_2$ at pH = 7 (equivalent to -0.59 V vs. normal hydrogen electrode (NHE) at pH = 7). Based on the above UV-Vis diffuse reflectance measurements of $Bi_{24}O_{31}Cl_{10}$, we can determine that its valence band potential should be 2.21 V. This suggests that $Bi_{24}O_{31}Cl_{10}$ could be sensitized by dyes in photochemical reactions. In previous studies, the redox potentials of RhB and RhB* were reported to be 0.95 and -1.42 V vs NHE, respectively[44]. As illustrated in Figure 3(d), the energy level of the excited RhB* locates well above the CB of $Bi_{24}O_{31}Cl_{10}$, which in turn favors the electron injection from the dye to the photocatalyst. As a result, the photoinduced electrons of RhB on the RhB* can migrate easily to the CB of $Bi_{24}O_{31}Cl_{10}$, which represents a typical dye sensitization process (Figure 3(d) inset).

As shown in Figure 3(e), the $Bi_{24}O_{31}Cl_{10}$ sample exhibits a transient photoresponse to visible light, suggesting that absorption of light generates photo-induced charge carriers in $Bi_{24}O_{31}Cl_{10}$ and leads to a significant photocurrent. The photon absorption process was further investigated by surface photovoltage spectroscopy (SPV), as shown in Figure 3(f). The broad peak in the UV and visible light region (300–520 nm) reveals an effective separation of photo-induced electron-hole pairs
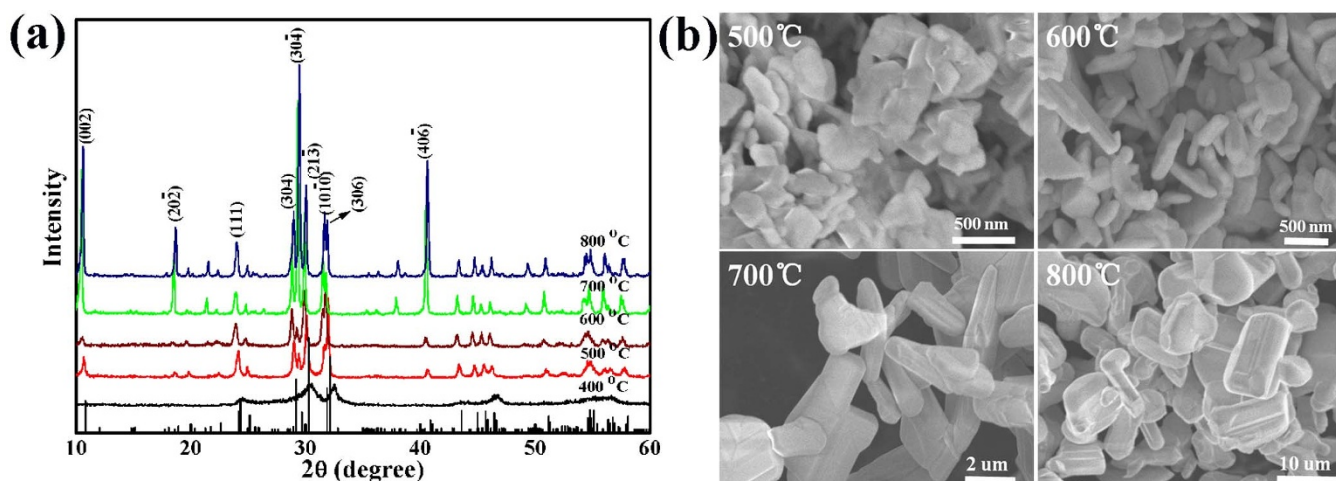
Figure 2 | (a) XRD patterns of $Bi_{24}O_{31}Cl_{10}$ samples calcined at different temperatures. (b) SEM images of plate-like $Bi_{24}O_{31}Cl_{10}$ calcined at 500, 600, 700 and 800°C. The scale bars represent 0.5 μm for (a) and (b), and 2 μm and 10 μm for (c) and (d), respectively.
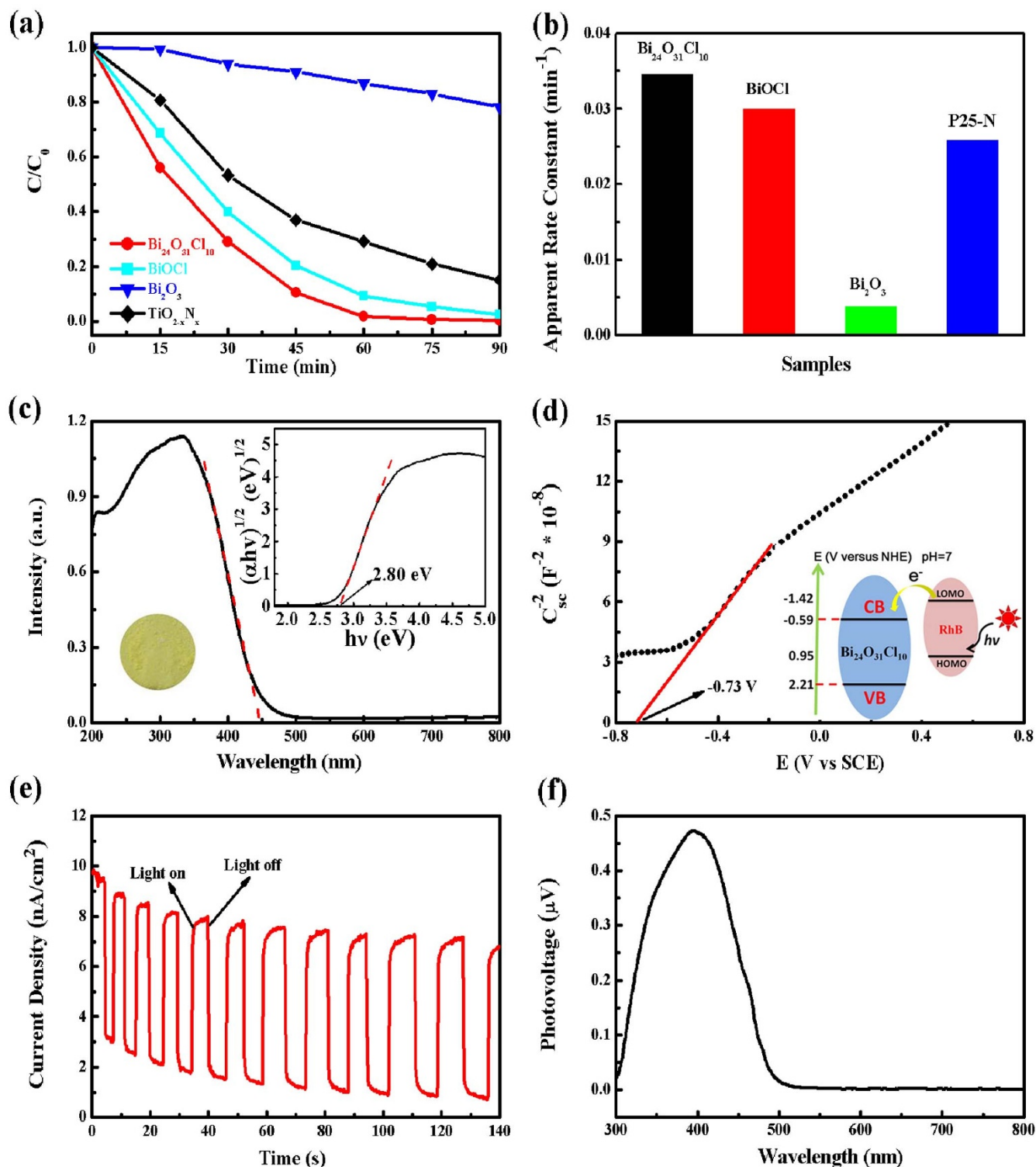
Figure 3 | (a) Decoloration of RhB over $Bi_{24}O_{31}Cl_{10}$, BiOCl, Bi_2O_3 and $Ti_{2-x}O_x$ (C/C_0-time curve). (b) Apparent rate constant of different samples. (c) UV-Vis diffuse reflectance spectrum of $Bi_{24}O_{31}Cl_{10}$ submicron platelets. The inset plot indicates that the band gap is 2.8 eV which is derived from diffuse reflectance spectrum. (d) Mott-Schottky plot for $Bi_{24}O_{31}Cl_{10}$ in 0.1 M Na_2SO_4 aqueous solution (pH = 7). The flat band potential is determined to be about −0.73 V. Inset shows a schematic diagram of the dye sensitization process in $Bi_{24}O_{31}Cl_{10}$/RhB. (e) Current density transient with light ON/OFF for $Bi_{24}O_{31}Cl_{10}$ powders under visible light ($\lambda \geq 420$ nm). (f) Surface photovoltage spectrum of $Bi_{24}O_{31}Cl_{10}$, which shows the largest photovoltage response in visible-light range.

under irradiation. The maximum photovoltage is achieved at an excitation wavelength of 405 nm, which is consistent with the band gap of 2.80 eV. Both the photocurrent response and the SPV characterizations corroborate the importance of the $Bi_{24}O_{31}Cl_{10}$ electronic structure in photocatalysis. In fact, the dispersive nature of the VB and CB, as well as the direct band gap are responsible for the highly photocatalytic performance of this *p*-block compound.

Photosensitivity of $Bi_{24}O_{31}Cl_{10}$. From the de-coloration of RhB over $Bi_{24}O_{31}Cl_{10}$ submicron platelets in visible light (Figure 4(a)), it was found that the absorptive intensity of RhB at a wavelength of 554 nm gradually decreases. The absorption band shifts to the shorter wavelength of 498 nm. This phenomenon reflects a typical process of photochemical N-de-ethylation of RhB to Rhodamine[17]. As the reaction time is increased above 75 min, the intensity of the absorption peak of Rhodamine (498 nm) continues to decrease, even though no peak shifting was observed. This indicates that the aromatic chromophore is still attacked by the active species leading to the decomposition of RhB[45]. This photocatalytic behaviour of $Bi_{24}O_{31}Cl_{10}$ reflects intense photosensitization activity similar to that of another bismuth oxyhalide, BiOCl[46]. In order to confirm the photosensitization process in RhB/$Bi_{24}O_{31}Cl_{10}$, a 300 W Xe lamp with a monochromatic light filter with the pass wavelength of 550 nm (see Supplementary Figure S7) was used for the irradiation light in a photocatalytic measurement, as shown in Figure 4(b) and 4(c). Note that RhB was still degraded, although $Bi_{24}O_{31}Cl_{10}$ cannot absorb light with a wavelength of 550 nm. We rule out possible physical adsorption because the absorption peaks show an obvious shift during the photocatalytic process which indicates a chemical process. Figure 4(d) shows the fluorescence emission spectra of RhB with and without $Bi_{24}O_{31}Cl_{10}$. The original RhB solution has a strong fluorescence emission at 580 nm (excited at 532 nm). When $Bi_{24}O_{31}Cl_{10}$ colloidal suspension was added into the RhB solution, it can be seen that the fluorescence emission is remarkably decreased. The fluorescence quenching indicates that the excited electrons have not gone back to the internal energy level in RhB, instead they are transferred directly from the LUMO of RhB to the CB of $Bi_{24}O_{31}Cl_{10}$[47]. This charge transfer was also confirmed by a photocurrent response measurement carried out on the $Bi_{24}O_{31}Cl_{10}$ and $Bi_{24}O_{31}Cl_{10}$/RhB samples by using visible light ($\lambda \geq$ 420 nm) and monochromatic light (550 nm) irradiation. Figure 4(e) shows a comparison of the photocurrent responses contributed by the $Bi_{24}O_{31}Cl_{10}$ and $Bi_{24}O_{31}Cl_{10}$/RhB samples. $Bi_{24}O_{31}Cl_{10}$/RhB shows a much stronger photocurrent under visible light irradiation. The photocurrent of the $Bi_{24}O_{31}Cl_{10}$/RhB gradually decreases in the cycling test because of photocatalytic degradation of RhB by $Bi_{24}O_{31}Cl_{10}$. On the other hand, the $Bi_{24}O_{31}Cl_{10}$/RhB sample produces obvious photocurrent under monochromatic light irradiation, while the $Bi_{24}O_{31}Cl_{10}$ does not show any photoresponse. The photoresponse characterizations clearly demonstrate that $Bi_{24}O_{31}Cl_{10}$ can be sensitized by dye molecules. Finally, the separation of photoinduced electron-hole pairs and charge transfer processes in $Bi_{24}O_{31}Cl_{10}$/RhB were investigated by typical electrochemical impedance spectroscopy (EIS). The slope of EIS plots can be used to evaluate the efficiency of charge separation and transfer. A smaller slope reflects higher electron-hole separation and transfer efficiencies, and vice versa[48,49]. The EIS Nyquist plot of a $Bi_{24}O_{31}Cl_{10}$/RhB film on indium tin oxide (ITO) electrodes measured in the dark shows an even smaller slope in contrast to that of $Bi_{24}O_{31}Cl_{10}$ measured under light irradiation, as displayed in Figure 4(f). This confirms that RhB indeed promotes the separation and transfer processes of photoinduced charge carriers in $Bi_{24}O_{31}Cl_{10}$/RhB in visible light.

Prospective applications. Due to its excellent photosensitive activity, $Bi_{24}O_{31}Cl_{10}$ is expected to be a candidate photoanode material in DSSCs. Indeed, $Bi_{24}O_{31}Cl_{10}$ has a proper energy level that matches the N719 (Supplementary Figure S8), which is a common dye-sensitizer in DSSCs[50]. The photovoltaic properties of a DSSC with $Bi_{24}O_{31}Cl_{10}$ as the photoelectrode were investigated. In order to identify the effects of dye photosensitivity, we also assessed a DSSC device with $Bi_{24}O_{31}Br_{10}$. Our previous results[9] show that $Bi_{24}O_{31}Br_{10}$ material has the same crystal structure and particle morphology as those of $Bi_{24}O_{31}Cl_{10}$ and it also show high

photocatalytic activity towards RhB degradation. Most importantly, the degradation of RhB by $Bi_{24}O_{31}Br_{10}$ is a hole oxidation process rather than a dye-sensitized process which is different with that of $Bi_{24}O_{31}Cl_{10}$. Figure 5(a) shows the schematic diagram of DSSC mechanism associated with a dye (N719) sensitized $Bi_{24}O_{31}Cl_{10}$ photoanode. The photocurrent density-voltage (J-V) curves of $Bi_{24}O_{31}Cl_{10}$ and $Bi_{24}O_{31}Br_{10}$ based DSSCs are shown in Figure 5(b). It can be found that the overall energy conversion efficiency (η) and the short-circuit photocurrent density (J_{sc}) of $Bi_{24}O_{31}Cl_{10}$ were much higher than those of $Bi_{24}O_{31}Br_{10}$. Incident photon-to-electron conversion efficiency (IPCE) is defined as the number of electrons collected per incident photon. The IPCE spectra (Figure 5(b)) for dye-sensitized solar cell show both materials electrons can be excited by light in range of 300–470 nm. The range of performance is mainly ascribed to ordinary band-gap photoexcitation and devices made with $Bi_{24}O_{31}Cl_{10}$ possess the same marginal peak IPCE values with that of $Bi_{24}O_{31}Br_{10}$ devices. The higher IPCE value of $Bi_{24}O_{31}Cl_{10}$ compared to $Bi_{24}O_{31}Br_{10}$ away from the dye peak absorbance wavelength (about 540 nm, as marked with '*' in the figure) can be attributed to its excellent dye-sensitized capacity[37]. The efficiencies of DSSCs with $Bi_{24}O_{31}Cl_{10}$ photoanodes are significantly higher than those reported for other DSSCs with BiOX (Cl, Br, I) materials as photoanodes[51,52].

In summary, a new visible-light photocatalyst $Bi_{24}O_{31}Cl_{10}$ has been explored through band-gap engineering of p-block bismuth oxide halides. $Bi_{24}O_{31}Cl_{10}$ shows high visible-light photocatalytic activity towards dye degradation, which is attributed to its narrow band gap, dispersive band structure and high quantum conversion efficiency. The photocatalytic properties of $Bi_{24}O_{31}Cl_{10}$ can be further enhanced by dye sensitization. Moreover, $Bi_{24}O_{31}Cl_{10}$ could be a suitable material for DSSC photoanodes because it exhibits proper energy level matching to the dye molecules. Our results suggest that it is promising to explore visible-light-active photocatalysts and photovoltaic materials through band-gap engineering of p-block element compounds.

Methods

Materials. $Bi(NO_3)_3 \cdot 5H_2O$, HNO_3, NaOH and cetyl trimethyl ammonium chloride (CTAC) were purchased from Sinopharm Chemical Reagent Co., Ltd. (SCRC). The model pollutant Rhodamine B (RhB) was obtained from Beijing Chemical Reagents Company. All reagents used in this work were of analytical grade and were used as received without any further purification.

Sample preparation. $Bi_{24}O_{31}Cl_{10}$ powders were synthesized by a chemical precipitation method. 2.42 g $Bi(NO_3)_3 \cdot 5H_2O$ was dissolved in 50 mL 1.6 M dilute nitric acid, and 0.6667 g CTAC was dissolved in 200 mL 0.14 M NaOH aqueous solution. The alkali solution was slowly dropped into the acid solution under vigorous magnetic stirring, and a white precipitate was formed at the same time. After the precipitate was purified by filtration, washed with distilled water several times, and heated at different heat-treatment temperatures (400°C, 500°C, 600°C, 700°C, and 800°C), yellow-green $Bi_{24}O_{31}Cl_{10}$ powders were obtained.

Structure characterization. Powder XRD patterns were collected with a PANalytical X′ Pert Pro X-ray diffractometer using Cu K*a* radiation (1.54 Å) and the working voltage of 40 kV. UV-Vis diffuse reflectance spectra were collected on a Cintra-10e spectrometer using $BaSO_4$ as the reference sample. The morphologies of the as-prepared samples were observed using a Hitachi SEM-CS 3400 operated at 10 kV. XPS was conducted at the Photoelectron Spectroscopy Station (Beamline 4W9B) of the Beijing Synchrotron Radiation Facility of the Institute of High Energy Physics, Chinese Academy of Sciences.

In the photocurrent-time response studies, a 300 W Xe lamp with a monochromator and a cut-off filter ($\lambda \geq$ 420 nm) was used as the light source, and the photocurrent as a function of irradiation time under visible light was collected by a KEITHLEY 2400 source meter. The SPV spectroscopy apparatus is composed of a source of monochromatic light, a lock-in amplifier (SR830-DSP) with a light chopper (SR540), and a photovoltaic cell. A 500 W xenon lamp (CHFXQ500W, Global Xenon Lamp Power) and a grating monochromator (Omni-5007, No.09010, Zolix) provided monochromatic light. The construction of the photocurrent-time response cell and the photovoltaic cell was in the form of a sandwich-like structure of indium tin oxide (ITO)-sample-ITO.

The photocurrent, EIS and Mott-Schottky measurements were conducted on an electrochemistry workstation (CHI-660D, China). $Bi_{24}O_{31}Cl_{10}$ film, Pt foil, saturated calomel electrode (SCE) and saturated 0.1 M Na_2SO_4 solution were used as the
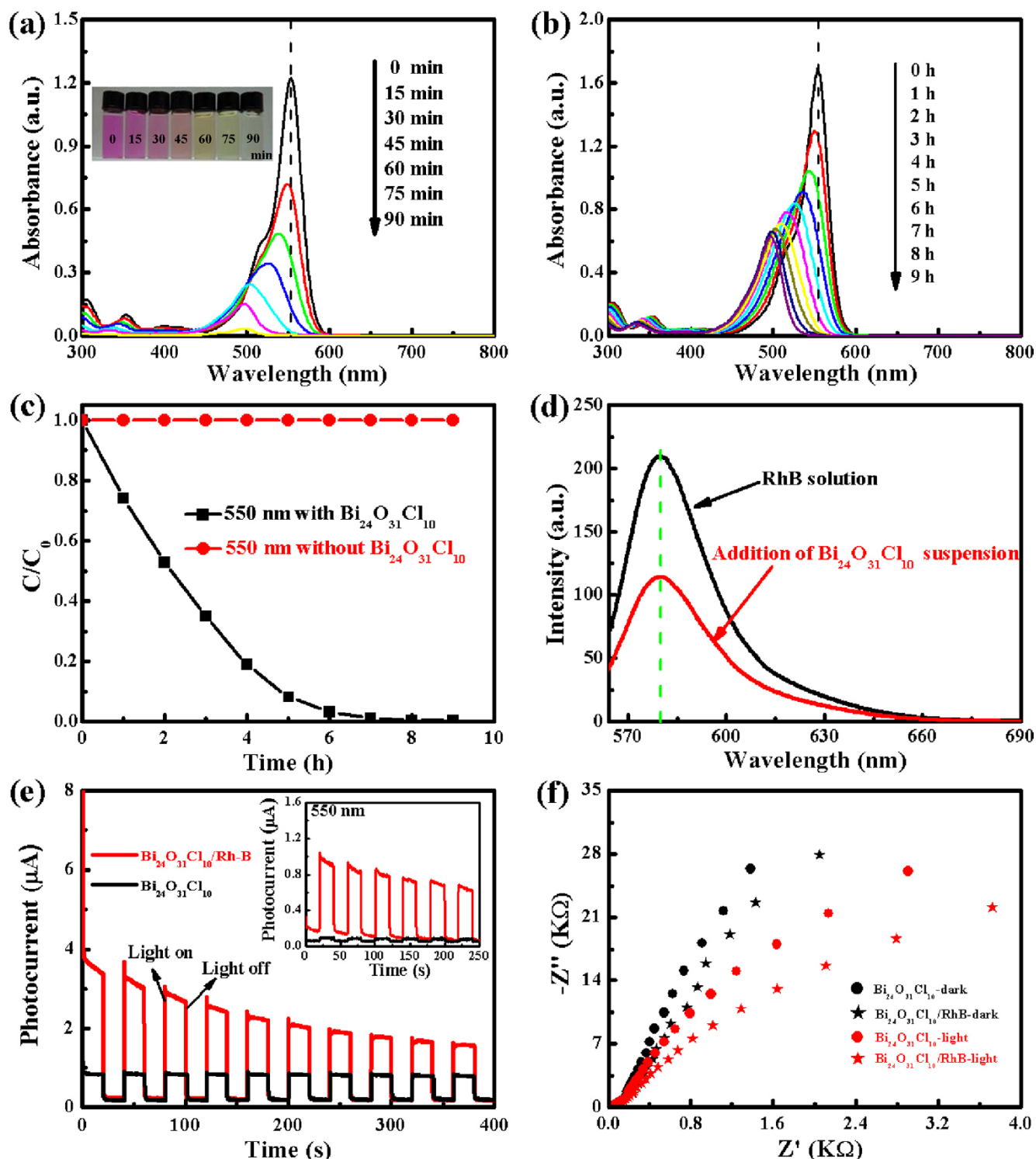
Figure 4 | (a) Photo-degradation of RhB over the $Bi_{24}O_{31}Cl_{10}$ sample under visible light ($\lambda \geq 420$ nm) over 90 min. Inset is color evolution of RhB corresponding to the degradation time. (b) Photodecomposition of RhB on $Bi_{24}O_{31}Cl_{10}$ under monochromatic light ($\lambda = 550$ nm) in over 9 hours. (c) Concentration changes of RhB with and without $Bi_{24}O_{31}Cl_{10}$ under monochromatic light ($\lambda = 550$ nm). (d) Fluorescence emission spectra of RhB solution and $Bi_{24}O_{31}Cl_{10}$/RhB suspension indicating a fluorescence quenching effect due to $Bi_{24}O_{31}Cl_{10}$. (e) Transient photocurrent response of $Bi_{24}O_{31}Cl_{10}$ and $Bi_{24}O_{31}Cl_{10}$/RhB under visible light irradiation. The inset shows the photocurrent responses of $Bi_{24}O_{31}Cl_{10}$ and $Bi_{24}O_{31}Cl_{10}$/RhB under monochromatic light at 550 nm. (f) Nyquist impedance plots of $Bi_{24}O_{31}Cl_{10}$ and $Bi_{24}O_{31}Cl_{10}$/RhB in the dark and under visible light ($\lambda \geq 420$ nm) conditions.

working, counter, the reference electrodes and the electrolyte respectively. The working electrode was prepared via the dip-coating method. Time-dependent photocurrent curves were measured by the amperometric *i-t* curve method. The Mott-Schottky measurements were monitored at a fixed frequency of 100 Hz with 10 mV amplitude at various potentials.

Photocatalytic reactions. Photodegradation of RhB dye: The catalyst (100 mg) was added to an aqueous solution of RhB (0.02 mmol/L, 100 mL) in a 150 mL quartz reactor. The photocatalytic experiments were carried out under irradiation by a 300 W Xe lamp with a filter glass ($\lambda \geq 420$ nm) to remove UV. Before the light experiments, dark adsorption experiments were carried out for 240 min. The
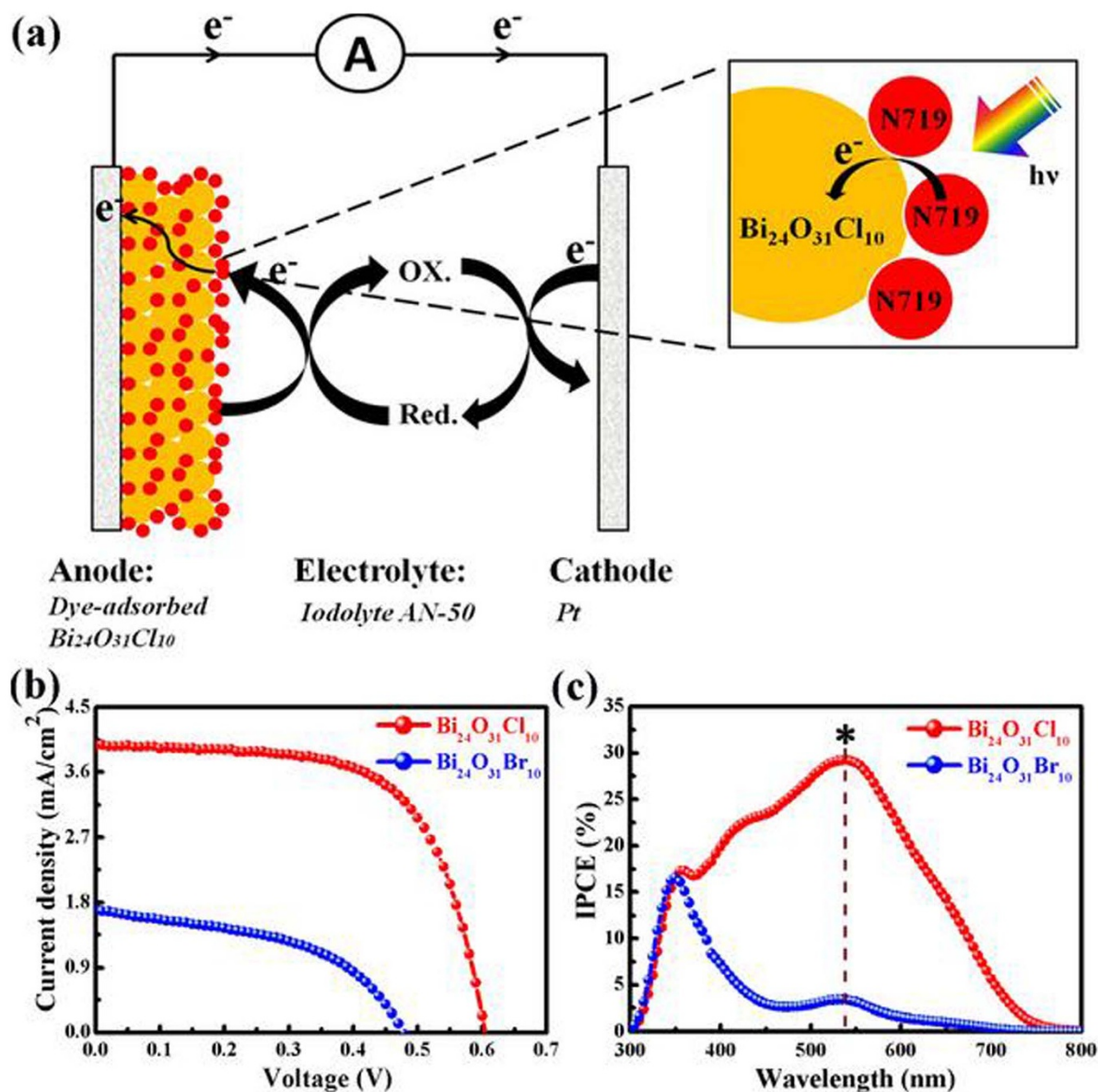
Figure 5 | (a) The schematic illustration of DSSC mechanism associated with a dye (N719) sensitized $Bi_{24}O_{31}Cl_{10}$ photoanode. (b) Current density-voltage (*J-V*) characteristics and (c) IPCE spectrum of a DSSC with N719-sensitized $Bi_{24}O_{31}Cl_{10}$ photoanode under solar light illumination compared with that of a DSSC with $Bi_{24}O_{31}Br_{10}$ photoanode.

absorption spectra of RhB were collected on a HITACHI U3010 UV-Vis spectrophotometer.

Assembly and testing of dye-sensitized solar cells. Dye absorption was carried out by immersing fluorine doped tin oxide (FTO) substrates loaded with the $Bi_{24}O_{31}Cl_{10}$ into ethanol-based commercial N719 dye solution at 25°C for 24 h. The dye adsorption amount was determined by measuring the UV-Vis absorption spectrum after the photoanodes were immersed in a dye-desorbing solution, 5 mL 0.01 M NaOH solution. The solar cells were prepared by assembling a Pt counter-electrode and a dye-adsorbed photoanode made from the $Bi_{24}O_{31}Cl_{10}$, and then sealing the assembly by using a Surlyn (Dupont) thermoplastic frame (25 μm thick). The assembled cell was filled with a commercial electrolyte purchased from Solaronix (Iodolyte AN-50), and then the cell was sealed again. Photocurrent density-voltage (*J-V*) characteristics were collected by exposing the cell to air mass (AM) 1.5 simulated sunlight from a solar simulator (PEL-L12, Peccell Technologies, Japan) combined with a Keithley 2400 source meter. The IPCE was measured as an action spectrum, and an optical fiber (3 mm diameter) was used for monochromatic irradiation (PEC-S20DC, Peccell Technologies, Japan). The monochromatic photocurrent was monitored by the continuous irradiation (dc measurement) method.

Theoretical calculations. The calculations were carried out using the Vienna *ab initio* simulation package (VASP) based on density functional theory with the projector-augmented wave (PAW) pseudopotential method. The exchange and correlation energy was treated via the generalized gradient approximation (GGA) using the Perdew-Burke-Emzerhof formulation. A conjugate-gradient algorithm was used to relax the ions into their ground states, and the energies and the forces on each ion were converged within $1.0 o t^{-6}$ eV/atom and 0.01 eV/Å, respectively. The Koln-Sham orbitals were expanded by a plane wave basis set, and an energy cut-off of 400 eV was used throughout. The Brillouin-zone integration was performed by using the Gamma-centered Monkhorst-Pack scheme with $1 \times 5 \times 2$ k-points, together with a Gaussian smearing broadening of 0.2 eV.

1. Carey, J. H., Lawrence, J. & Tosine, H. M. Photodechlorination of PCB's in the presence of titanium dioxide in aqueous suspensions. *Bull. Environ. Contam. Toxicol.* **16**, 697–701 (1976).
2. Mills, A., Davies, R. H. & Worsley, D. Water purification by semiconductor photocatalysis. *Chem. Soc. Rev.* **22**, 417–425 (1993).
3. Legrini, O., Braun, A. M. & Oliveros, E. Photochemical processes for water treatment. *Chem. Rev.* **93**, 671–698 (1993).
4. Zou, Z. G., Ye, J. H., Sayama, K. & Arakawa, H. Direct splitting of water under visible light irradiation with an oxide semiconductor photocatalyst. *Nature* **414**, 625–627 (2001).
5. Liu, Q. *et al.* High-yield synthesis of ultralong and ultrathin Zn_2GeO_4 nanoribbons toward improved photocatalytic reduction of CO_2 into renewable hydrocarbon fuel. *J. Am. Chem. Soc.* **132**, 14385–14387 (2010).

6. Chen, X. B. & Mao, S. S. Titanium dioxide nanomaterials: Synthesis, Properties, Modifications, and Applications. *Chem. Rev.* **107**, 2891–2959 (2007).

7. Zhou, J. *et al.* Growth rate controlled synthesis of hierarchical Bi_2S_3/In_2S_3 core/shell microspheres with enhanced photocatalytic activity. *Sci. Rep.* **4**, 4027 (2014).

8. Wang, X. C. *et al.* A metal-free polymeric photocatalyst for hydrogen production from water under visible light. *Nature Materials* **8**, 76–80 (2009).

9. Shang, J. *et al.* Bismuth oxybromide with reasonable photocatalytic reduction activity under visible light. *ACS Catal.* **4**, 954–961 (2014).

10. Yang, S. *et al.* Exfoliated graphitic carbon nitride nanosheets as efficient catalysts for hydrogen evolution under visible light. *Adv. Mater.* **25**, 2452–2456 (2013).

11. Chen, X. B. & Clemens, B. The electronic origin of the visible-light absorption properties of C-, N- and S-doped TiO_2 nanomaterials. *J. Am. Chem. Soc.* **130**, 5018–5019 (2008).

12. Ouyang, S. X. *et al.* A systematical study on photocatalytic properties of $AgMO_2$ (M = Al, Ga, In): effects of chemical compositions, crystal structures, and electronic structures. *J. Phys. Chem. C* **113**, 1560–1566 (2009).

13. Umezawa, N., Ouyang, S. X. & Ye, J. H. Theoretical study of high photocatalytic performance of Ag_3PO_4. *Phys. Rev. B* **83**, 035202 (2011).

14. Wang, X. L. *et al.* Proposal for a new class of materials: Spin gapless semiconductors. *Phys. Rev. Lett.* **100**, 156404 (2008).

15. Vurgaftman, I., Meyer, J. R. & Ram-Mohan, L. R. Band parameters for III–V compound semiconductors and their alloys. *J. Appl. Phys.* **89**, 5815–5875 (2001).

16. Santander-Syro, A. F. *et al.* Two-dimensional electron gas with universal subbands at the surface of $SrTiO_3$. *Nature* **469**, 189–193 (2011).

17. Watanabe, T., Takirawa, T. & Honda, T. Photocatalysis through excitation of adsorbates. 1. Highly Efficient N-deethylation of Rhodamine B adsorbed to CdS. *J. Phys. Chem.* **81**, 1845–1851 (1977).

18. O'regan, B. *et al.* A low-cost, high-efficiency solar cell based on dye-sensitized. *Nature* **353**, 737–740 (1991).

19. Moser, J. & Graetzel, M. Photosensitized electron injection in colloidal semiconductors. *J. Am. Chem. Soc.* **106**, 6557–6564 (1984).

20. He, R. A., Cao, S. W., Zhou, P. & Yu, J. G. Recent advances in visible light Bi-based photocatalysts. *Chin. J. Catal.* **35**, 989–1007 (2014).

21. Zhang, L. *et al.* Sonochemical synthesis of nanocrystallite Bi_2O_3 as a visible-light-driven photocatalyst. *Appl. Catal. A* **308**, 105–110 (2006).

22. Tang, J. & Alivisatos, A. P. Crystal splitting in the growth of Bi_2S_3. *Nano Lett.* **6**, 2701–2706 (2006).

23. Fu, H. B., Pan, C. S., Yao, W. Q. & Zhu, Y. F. Visible-light-induced degradation of rhodamine B by nanosized Bi_2WO_6. *J. Phys. Chem. B* **109**, 22432–22439 (2005).

24. Wan, Z. & Zhang, G. K. Controlled synthesis and visible light photocatalytic activity of $Bi_{12}GeO_{20}$ uniform microcrystals. *Sci. Rep.* **4**, 6298 (2014).

25. Yao, W. F. *et al.* Synthesis and photocatalytic property of bismuth titanate $Bi_4Ti_3O_{12}$, *Mater. Lett.* **57**, 1899–1902 (2003).

26. Bi, J. *et al.* Simple solvothermal routes to synthesize nanocrystalline Bi_2MoO6 photocatalysts with different morphologies. *Acta Materialia* **55**, 4699–4705 (2007).

27. Yu, J. & Kudo, A. Effects of Structural Variation on the Photocatalytic Performance of Hydrothermally Synthesized $BiVO_4$. *Adv. Funct. Mater.* **16**, 2163–2169 (2006).

28. Zheng, Y. *et al.* Synthetic $Bi_2O_2CO_3$ nanostructures: Novel photocatalyst with controlled special surface exposed. *J. Mol. Catal. A-Chem.* **317**, 34–40 (2010).

29. Guan, X. *et al.* Vacancy associates promoting solar-driven photocatalytic activity of ultrathin bismuth oxychloride nanosheets. *J. Am. Chem. Soc.* **135**, 10411–10417 (2013).

30. Lin, X. P., Huang, T., Huang, F. Q., Wang, W. D. & Shi, J. L. Photocatalytic activity of a Bi-based oxychloride Bi_3O_4Cl. *J. Phys. Chem. B* **110**, 24629–24634 (2006).

31. Xiao, X. Y., Jiang, J. & Zhang, L. Z. Selective oxidation of benzyl alcohol into benzaldehyde oversemiconductors under visible light: the case of $Bi_{12}O_{17}Cl_2$ nanobelts. *Appl. Catal. B: Environ.* **142–143**, 487–493 (2013).

32. Sun, W. *et al.* Visible light-induced efficient contaminant removal by Bi_5O_7I. *Environ. Sci. Technol.* **43**, 2005–2010 (2009).

33. Kako, T., Zou, Z. G., Katagiri, M. & Ye, J. H. Decomposition of organic compounds over $NaBiO_3$ under visible light irradiation. *Chem. Mater.* **19**, 198–202 (2007).

34. Ramachandran, R. *et al.* Photocatalytic properties of $KBiO_3$ and $LiBiO_3$ with tunnel structures. *J. Chem. Sci.* **123**, 517–524 (2011).

35. Yu, X., Zhou, J., Wang, Z. & Cai, W. Preparation of visible light-responsive $AgBiO_3$ bactericide and its control effect on the Microcystis aeruginosa. *J. Photoch. Photobio. B* **101**, 265–270 (2010).

36. Xiao, X. *et al.* Oxygen-rich bismuth oxyhalides: Generalized one-pot synthesis, band structures and visible-light photocatalytic properties. *J. Mater. Chem.* **22**, 22840–22843 (2012).

37. Cheng, H. F., Huang, B. B. & Dai, Y. Engineering BiOX (X = Cl, Br, I) nanostructures for highly efficient photocatalytic applications. *Nanoscale* **6**, 2009–2026 (2014).

38. Eggenweiler, U., Keller, E. & Kraemer, V. Redetermination of the crystal structures of the "Arppe compound", $Bi_{24}O_{31}Cl_{10}$, and the isomorphous $Bi_{24}O_{31}Br_{10}$. *Acta Cryst. B* **56**, 431–437 (2000).

39. Pauling, L. *The Nature of the Chemical Bond and the Structure of Molecules and Cystal: An Introduction to Modern Structural Chemistry*. pp 113–114 (Cornell University Press, New York, 1960).

40. Ai, Z., Ho, W., Lee, S. & Zhang, L. Efficient photocatalytic removal of NO in indoor air with hierarchical bismuth oxybromide nanoplate microspheres under visible light. *Environ. Sci. Technol.* **43**, 4143–4150 (2009).

41. Butler, M. A. Photoelectrolysis and physical properties of the semiconducting electrode WO_3. *J. Appl. Phys.* **48**, 1914–1920 (1977).

42. Weng, S. X., Chen, B. B., Xie, L. Y., Zheng, Z. Y. & Liu, P. Facile in situ synthesis of a Bi/BiOCl nanocomposite with high photocatalytic activity. *J. Mater. Chem. A* **1**, 3068–3075 (2013).

43. Kong, D. S. The influence of fluoride on the physicochemical properties of anodic oxide films formed on titanium surfaces. *Langmuir* **24**, 5324–5331 (2008).

44. Zhao, L. L., Xiong, Z. G. & Zhao, X. S. Pillaring chemically exfoliated graphene oxide with carbon nanotubes for photocatalytic degradation of dyes under visible light irradiation. *ACS Nano* **4**, 7030–7036 (2010).

45. Wang, Q., Chen, C., Zhao, D., Ma, W. & Zhao, J. Change of adsorption modes of dyes on fluorinated TiO_2 and its effect on photocatalytic degradation of dyes under visible irradiation. *Langmuir* **24**, 7338–7345 (2008).

46. Wang, D. H. *et al.* Nanosheet-constructed porous BiOCl with dominant {001} facets for superior photosensitized degradation. *Nanoscale* **4**, 7780–7785 (2012).

47. Hu, J. L., Fan, W. J., Ye, W. Q., Huang, C. J. & Qiu, X. Q. Insights into the photosensitivity activity of BiOCl under visible light irradiation. *Appl. Catal. B: Environ.* **158–159**, 182–189 (2014).

48. Bai, X. J., Wang, L., Zong, R. L. & Zhu, Y. F. Photocatalytic activity enhanced via g-C_3N_4 nanoplates to nanorods. *J. Phys. Chem. C* **117**, 9952–9961 (2013).

49. Zhu, Y. Y. *et al.* Enhancement of photocatalytic activity for $BiPO_4$ via phase junction. *J. Mater. Chem. A* **2**, 13041–13048 (2014).

50. Mishra, A., Fischer, M. K. R. & Bäuerle, P. Metal-free organic dyes for dye-sensitized solar cells: From structure property relationships to design rules. *Angew. Chem. Int. Ed.* **48**, 2474–2499 (2009).

51. Luz, A., Conradt, J., Wolff, M., Kalt, H. & Feldmann, C. *p*-DSSCs with BiOCl and BiOBr semiconductor and polybromide electrolyte. *Solid State Sciences* **19**, 172–177 (2013).

52. Wang, K. W., Jia, F. L., Zheng, Z. & Zhang, L. Z. Crossed BiOI flake array solar cells. *Electrochem. Commun.* **12**, 1764–1767 (2010).

Acknowledgments

Author contributions

W.C.H. and T.M.W. designed the experiments. L.W., J.S., S.H.H and W.C.H. performed the experimental work and collected and analyzed the data. W.C.H., S.Q.J. and Y.D., carried out the first-principles calculations and theoretical analysis. Z.Q.S. and S.X.D. assembled and tested the dye-sensitized solar cells. T.F.X. and D.J.W. were responsible for the surface potential spectroscopy analysis. J.O.W. carried out the XPS characterization and helped with data analysis. W.C.H., L.W. and Y.D. analyzed the data and wrote the paper.

Additional information